

UKAEA-CCFE-PR(25)399

P. Srinivasan, S. Puri, K.P. Dominguez, A.P. Horsfield,  
M.R. Gilbert, D. Nguyen-Manh

# **Atomic cluster expansion interatomic potentials for lithium: Investigating the solid and liquid phases**

Enquiries about copyright and reproduction should in the first instance be addressed to the UKAEA Publications Officer, Culham Science Centre, Building K1/O/83 Abingdon, Oxfordshire, OX14 3DB, UK. The United Kingdom Atomic Energy Authority is the copyright holder.







The contents of this document and all other UKAEA Preprints, Reports and Conference Papers are available to view online free at [scientific-publications.ukaea.uk/](https://scientific-publications.ukaea.uk/)

# **Atomic cluster expansion interatomic potentials for lithium: Investigating the solid and liquid phases**

P. Srinivasan, S. Puri, K.P. Dominguez, A.P. Horsfield, M.R. Gilbert,  
D. Nguyen-Manh



## Atomic cluster expansion interatomic potentials for lithium: Investigating the solid and liquid phases

Prashanth Srinivasan <sup>1,\*</sup> Siddharth Puri <sup>2</sup> Karen Pacho Dominguez <sup>2</sup> Andrew P. Horsfield <sup>2,1</sup>  
Mark R. Gilbert <sup>1,3</sup> and Duc Nguyen-Manh <sup>1,3</sup>

<sup>1</sup>*United Kingdom Atomic Energy Authority, Culham Campus, Abingdon OX14 3DB, United Kingdom*

<sup>2</sup>*Department of Materials, Imperial College London, South Kensington Campus, London SW7 2AZ, United Kingdom*

<sup>3</sup>*Department of Materials, University of Oxford, Oxford OX1 3PH, United Kingdom*



(Received 5 March 2025; revised 8 July 2025; accepted 22 July 2025; published 27 August 2025)

We develop an atomic cluster expansion (ACE) interatomic potential for lithium that accurately models both the solid and liquid phase and the corresponding melting point. The training data is obtained from 0 K density functional theory (DFT) and finite temperature *ab initio* molecular dynamics simulations of both solid and liquid Li. The ACE predicted properties for both phases obtained from molecular dynamics simulations are in close agreement with DFT and experimental data from the literature. The potential is able to capture the energy differences of the different competing phases of the solid at 0 K and finite temperature properties of the experimentally observed bcc phase. The potential also accurately predicts the temperature dependence of liquid density, viscosity, and the diffusion coefficient. The melting point is calculated using the two-phase coexistence method and is remarkably close to the experimental value. The potential is used to predict stress-induced phase transformations in solid Li and pressure-volume isotherms in liquid Li. We underline the necessity for a complete training set that includes both solid and liquid configurations in order to obtain a potential that precisely models both phases. By using the ACE formalism, we also systematically investigate the contributions of interactions involving  $N$  bodies and the number of radial parameters needed to separately represent both phases since they have a direct consequence on the computational cost of the potential. We shed light on the complexity of the ACE potential needed to model solid and liquid lithium efficiently.

DOI: [10.1103/q4nm-qyk4](https://doi.org/10.1103/q4nm-qyk4)

### I. INTRODUCTION

Lithium is being considered for two roles in fusion power plants: tritium breeding and cooling. Thus, to design and build sustainable fusion reactors, it is important to understand the behavior of Li and Li-based compounds. Liquid Li, liquid lithium-lead alloy, solid Li ceramics, and Li-based molten salts have been touted as prime candidates for tritium breeding [1,2]. An additional advantage of liquid Li is the possibility to use it as a coolant by absorbing the heat produced by the high neutron flux [3]. Outside of operational phases, for example during maintenance periods, the breeder material in a fusion reactor is allowed to cool down to room temperature and the liquid breeder materials then solidify. The liquid breeder materials can also locally solidify along the edges of the blanket at the interface with the surrounding structural material. Hence it becomes crucial to understand the temperature dependent behavior of both solid and liquid Li phases under a range of external conditions.

Several questions remain unanswered regarding the use of Li as a breeder, but of particular concern is how hydrogen isotopes can be stored and how they diffuse within the breeder. Achieving understanding by experimental means is possible, but the complexity of the system makes this very

expensive and difficult. Computational techniques such as atomistic simulations provide a safe, inexpensive, and flexible way to analyze and hence understand such systems under different conditions. However, the reliability of the results depends on the accuracy of the interatomic potential that drives the dynamics of the system. Further, the need for accuracy can require large simulation cells; thus we need computationally affordable potentials that can be scaled to bigger system sizes.

The phase diagram of solid Li across the temperature-pressure range is quite complex [4–6]. First principles density functional theory (DFT) predicts several energetically competing phases at 0 K with the face-centered cubic (fcc) as the lowest-energy structure [7] and body-centered cubic (bcc), hexagonal close-packed (hcp), and rhombohedral h9R structures only marginally higher in energy compared to the fcc phase [8]. However, the bcc phase becomes entropically stabilized at 100–200 K, making it the experimentally observed room temperature phase [8,9]. Under the application of external pressure at room temperature even as low as 10 GPa, the bcc phase transforms into the fcc phase [4–6].

Accurately capturing these tiny energy differences in an interatomic potential is a very challenging task. Nichol *et al.* [10] developed an EAM potential to study property trends in simple metals, including Li. In order to include angular terms in the formalism, Ko *et al.* [11] and Qin *et al.* [12] developed second-nearest neighbor modified embedded atom method (2NN-MEAM) potentials for predicting phase transitions in

\*Contact author: prashanth.srinivasan@ukaea.uk

solid Li. Besides empirical potentials, Phuthi *et al.* [13], Zuo *et al.* [14], and Wang *et al.* [15] trained machine-learning based interatomic potentials (MLIPs) to study bulk and surface properties of solid Li and high-pressure structures of solid Li, respectively. While all the above potentials predict the overall behavior of solid Li quite accurately, there are always certain properties that are more challenging to capture. For instance, some of the potentials fail to capture the bcc-fcc-h9R energy difference or accurate elastic constants of bcc and fcc phases. Nevertheless, none of the above potentials have explicitly been developed or trained to model liquid Li.

There have been relatively fewer attempts to develop interatomic potentials to model Li's liquid phase. In 2009, Belashchenko *et al.* [16] developed an embedded atom method (EAM) interatomic potential by fitting to experimental data above the melting point. Cui *et al.* [17] developed an improved second nearest neighbor modified embedded atom method (2NN-MEAM) potential which outperformed the EAM potential in accuracy. However, neither potential was able to predict accurate values for the temperature-dependent viscosity or the self-diffusion coefficient. More recently, Al-Awad *et al.* [18] developed an EAM potential that rectified these drawbacks. By introducing a long-range oscillatory form of the pair potential they were able to tune the potential to reproduce the experimental melting point and experimental densities and predicted other properties more accurately.

To realistically simulate different scenarios of a lithium breeder blanket, the interatomic model should be able to accurately predict both solid and liquid phases and the transformation. In order to do so, we require a functional form for the potential that can accommodate a more complete description of the local atomic environment than is possible with empirical potentials such as the EAM and the 2NN-MEAM. MLIPs provide us with the flexibility needed to model more complex atomic systems since they are derived from local atomic environment descriptors that span a larger parameter space. Several classes of MLIPs have garnered attention over the past two decades, each with their own sets of descriptors [19–29]. One such machine-learning based model is the atomic cluster expansion (ACE) interatomic potential [30]. The ACE potential provides a formally complete and efficient representation of properties as a function of local atomic environment using many-body functions. A general description and understanding of the ACE formalism has been presented in the Supplemental Material A [31] of this paper. The basis set used to represent atomic structures in the ACE formalism has been proven to be complete in several works in the literature [30,32,33]. The ACE formalism also allows one to systematically study the contribution of different many-body interactions in a given system. Hence, in this work, we develop an ACE MLIP to model the lithium system. We also analyze the effect of many-body contributions on solid and liquid lithium properties by training and comparing a set of ACE potentials that include different orders of many-body terms. MLIPs though, suffer from poor extrapolation of properties, for instance to temperatures or phases not included in the training, as discussed in the Supplemental Material B [31] for the case of Cu using a previously developed ACE potential [34]. Therefore, in the current work, we train the ACE potential for Li on 0 K DFT and finite temperature

*ab initio* molecular dynamics (AIMD) configurations that span both the solid and liquid phases.

The remainder of this manuscript is arranged as follows. The computational details for building the DFT training set, training the ACE potential, and performing molecular dynamics (MD) simulations are provided in Sec. II. In Sec. III we report the results for the final fitted potential when applied to both phases and compare them to DFT and experimental data. In Sec. IV, we discuss the contribution of many-body terms and perform a cost versus accuracy analysis of a set of potentials trained with different numbers of radial and angular parameters. The conclusions and outlook of this work are summarized in Sec. V.

## II. COMPUTATIONAL METHODS

### A. DFT training data

The ACE potential is trained on first principles calculations that use density functional theory (DFT). All DFT calculations are performed using the VASP code [35] within the projected augmented-wave (PAW) method [36,37]. For the results shown in the main text, the ACE is trained on DFT data that uses the generalized gradient approximation (GGA) exchange correlation (XC) functional by Perdew, Burke, and Ernzerhof (PBE) [38]. The effect of the XC functional is discussed in the Supplemental Material C [31], where results using the local density approximation (LDA) [39] XC functional are compared to those using GGA. Note that all the DFT calculations include only one valence electron for Li. Including additional valence electrons has a negligibly small effect on the properties, which is also outlined in the Supplemental Material C [31]. The Methfessel-Paxton smearing method [40] with a smearing width of 0.1 eV is used to approximate the orbital occupation function. The calculations for the training set are performed on 128-atom supercells (modified accordingly for vacancy, interstitial, and non-bcc structures) with a plane wave energy cutoff of 450 eV and a  $4 \times 4 \times 4$   $k$ -point grid.

The training set used to fit the ACE potential contains both solid and liquid configurations obtained from 0 K static DFT and finite temperature *ab initio* molecular dynamics (AIMD) simulations. The complete set of calculations is summarized in Table I. To sample the solid phase, we explicitly include 100 structures at 0 K spanning a volume range for each of the four energetically competing phases in the training set as given in Table I. We perform AIMD simulations of the bcc, fcc, and hcp phases at 400 K. For the bulk bcc phase, we perform these AIMD simulations for a set of six volumes and five each for the bulk fcc and hcp phases. We choose an additional smaller volume for the bcc phase to accurately capture high pressure configurations and the corresponding melting point. Additionally, we perform AIMD runs at 400 K and a set of volumes starting from the following modified bcc structures after relaxation: structures with different numbers of vacancies (one to four); a structure with a  $\langle 111 \rangle$  self-interstitial, which is the most stable self-interstitial atom (SIA) defective structure; a  $[100]$  and a  $[110]$  free surface. To sample the liquid phase, AIMD simulations are performed at five different temperatures and five volumes at each temperature.

TABLE I. Summary of the VASP calculations performed for the solid and liquid Li phases to generate configurations for the training data set. The first four rows correspond to 0 K DFT calculations. The remaining rows correspond to AIMD runs which are performed for 2000 steps in an *NVT* ensemble at the corresponding volume and temperature. The first 1000 steps are used for training and the last 1000 are used for validating the potential. One configuration in every 10 from the AIMD snapshots is chosen for the final training set, except for the fcc phase where one in every 5 is chosen. The supercell size is 128 atoms unless otherwise mentioned.

Solid configurations	Temperature (K)	Volume per ion ( $\text{\AA}^3$ )
bcc	0	16.54, 16.60, ..., 23.53 (100 volumes)
fcc (108 atoms)	0	17.61, 17.66, ..., 23.24 (100 volumes)
h9R (108 atoms)	0	14.80, 14.90, ..., 27.02 (100 volumes)
hcp (96 atoms)	0	14.66, 14.75, ..., 26.76 (100 volumes)
bcc bulk	400	16.90, 18.01, 19.16, 20.35, 21.60, 22.90
bcc with divacancy	400	18.01, 19.16, 20.35, 21.60, 22.90
bcc with trivacancy	400	18.01, 19.16, 20.35, 21.60, 22.90
bcc with quad vacancy	400	18.01, 19.16, 20.35, 21.60, 22.90
bcc with $\langle 111 \rangle$ SIA	400	16.95, 18.62, 20.40, 22.29
bcc with [100] surface	400	3 volumes ( $a = 2.82 \text{ \AA}$ , $2.97 \text{ \AA}$ , $3.12 \text{ \AA}$ )
bcc with [110] surface (144 atoms)	400	3 volumes ( $a = 2.82 \text{ \AA}$ , $2.97 \text{ \AA}$ , $3.12 \text{ \AA}$ )
fcc bulk (108 atoms)	400	16.88, 18.55, 20.33, 22.21
hcp bulk (144 atoms)	400	16.70, 18.35, 20.10, 21.97
Temperature (K)		Volume per ion ( $\text{\AA}^3$ )
Liquid configurations	600	19.62, 20.90, 22.24, 23.62, 25.07
	800	20.90, 22.24, 23.62, 25.07, 26.57
	1000	20.90, 22.24, 23.62, 25.07, 26.57
	1200	22.24, 23.62, 25.07, 26.57, 28.14
	1400	22.24, 23.62, 25.07, 26.57, 28.14

All AIMD simulations are run in the *NVT* ensemble for 2000 steps with a time step of 0.5 fs. Only the first 1000 steps are used for training. The last 1000 steps are used for validating the potential. In order to obtain uncorrelated snapshots, we pick one in every ten AIMD configurations for training the potential. However, for the bulk fcc phase, we choose one in every five configurations to indirectly increase the weight given to fcc structures. This improves the accuracy of the fitted potential when predicting the bcc-fcc-liquid phase transformations. Overall, the training data set contains 2500 liquid snapshots and 4700 solid snapshots.

### B. Atomic cluster expansion interatomic potential: Formalism

An overview of the formalism of the ACE interatomic potential is provided in this subsection. For a more detailed and general understanding of the ACE formalism, the reader is advised to refer to Supplemental Material A [31]. For a system with  $N$  atoms, the energy of the system can be represented as a sum of individual atomic energies, given by

$$E_{\text{tot}} = \sum_{i=1}^N E_i. \quad (1)$$

Each atomic energy is evaluated allowing interactions only with atoms within a certain cutoff range of the central atom. This locality of interactions provides a linear scaling with system size. The atomic energies  $E_i$  can be obtained from a combination of different atomic properties  $\varphi_i^{(p)}$ , which could, in principle, represent bonding, repulsion, etc. Hence  $E_i$  can generically be expressed as a nonlinear function given as

$$E_i = \mathcal{F}(\varphi_i^{(1)}, \varphi_i^{(2)}, \dots, \varphi_i^{(p)}). \quad (2)$$

A simple linear representation of the atomic energy means that  $E_i$  can be expressed as

$$E_i = \varphi_i. \quad (3)$$

However, for metallic systems, a faster convergence of the atomic energy with many-body interactions can sometimes be achieved by employing a nonlinear form representative of the Finnis-Sinclair potential [41], as given by

$$E_i = \varphi_i^{(1)} + \sqrt{\varphi_i^{(2)}}, \quad (4)$$

where  $\varphi_i^{(1)}$  and  $\varphi_i^{(2)}$  are representative of the pairwise repulsion and the embedding function. Within the ACE formalism, each  $\varphi_i^{(p)}$  can be expanded using a set of atomic descriptors given by

$$\varphi_i^{(p)} = \sum_{\mathbf{v}} c_{\mathbf{v}}^{(p)} \mathbf{B}_{\mathbf{v}}, \quad (5)$$

where  $c_{\mathbf{v}}^{(p)}$  is an expansion coefficient and  $\mathbf{B}_{\mathbf{v}}$  a basis function with multi-indices  $\mathbf{v}$ : see below for the component indices.

The building blocks for the ACE atomic descriptors are a set of orthogonal and complete single-bond basis functions  $\phi_{\mathbf{v}}(r_{ij})$ , expressed as

$$\phi_{\mathbf{v}}(r_{ij}) = R_{nl}(r_{ij}) Y_{lm}(\hat{\mathbf{r}}_{ji}), \quad (6)$$

where  $R_{nl}$  are radial functions that depend on the distance from atom  $i$  to atom  $j$ ,  $Y_{lm}$  are spherical harmonic functions depending on the direction  $\hat{\mathbf{r}}$ , and  $\mathbf{v} = (nlm)$  is a cumulative index. The complexity of the descriptor can be altered by choosing different values of  $n$  and  $l$  prior to training the potential. Choosing larger values provides more flexibility

enabling accurate training on larger data sets, but significantly increases the computational cost of using the potential to do MD simulations. The atomic base  $A$ , obtained by summing over all neighbors of the central atom, is expressed as

$$A_{iv} = \sum_j \phi_v(\mathbf{r}_{ji}), \quad (7)$$

following which basis functions  $A$  of different body orders  $T$  are constructed as

$$A_{iv} = \prod_{t=1}^T A_{iv_t}. \quad (8)$$

In Eq. (8), with every additional product, an additional term in the  $N$ -body decomposition of the atomic property can be parametrized and  $v$  is a cumulative index ( $\mathbf{n}\mathbf{l}\mathbf{m}$ ) in the product space of multiple spherical harmonics for different values of  $T$ . More specifically, only up to two-body interactions can be parametrized using  $t = 1$ . To account for three-body interactions, one needs to consider basis functions up to  $t = 2$ , and up to  $t = 3$  for four-body interactions, and so on. The basis functions in Eq. (8) need to be invariant under translation, rotation, inversion, and permutation. This can be achieved by creating invariant combinations  $B_{iv}$  from the original functions  $A_{iv'}$

$$B_{iv} = \sum_{v'} C_{vv'} A_{iv'}, \quad (9)$$

where the generalized Clebsch-Gordan coefficients  $C$  remove functions that are not rotationally invariant and  $v$  corresponds to the index ( $T\mathbf{n}\mathbf{l}$ ). We now have the final set of basis functions  $B_{iv}$  required for the expansion of an atomic property  $\varphi_i^{(p)}$  as given in Eq. (5).

For all figures and data discussed in the Results section of this manuscript, the interatomic potential that has been developed considers a Finnis-Sinclair type of energy expansion [Eq. (4)], where  $\varphi_i^{(1)}$  and  $\varphi_i^{(2)}$  are expanded within the ACE formalism. In the Discussion section, we compare and show the faster convergence of this potential to one that considers only a linear expansion of the atomic energy [Eq. (3)]. Additionally, we examine the effect of different many-body interactions [different values of  $T$  in Eq. (8)], the radial cutoff, and the effect of the index  $n$  in Eq. (6) on cost and accuracy of the results in the Discussion section.

### C. Atomic cluster expansion: Parametrization

The parameters of the ACE potential are fitted using the Pacemaker package [34,42,43]. A cutoff of 5.5 Å is chosen for all interactions, based on the range of DFT interactions. For the basis functions, up to four-body interactions [up to  $T = 3$  in Eq. (8)] are considered. The maximum value of the indices  $n$  and  $l$  for each order are summarized in Table II. Spherical Bessel-type functions are chosen to expand the radial part of the ACE formalism [ $R_{nl}(r_{ji})$  in Eq. (6)], which lead to 360 expansion coefficients. With the above chosen values for  $n$ ,  $l$ , and  $T$ , we end up with 403 basis functions for each cluster expansion  $\varphi_i^{(1)}$  and  $\varphi_i^{(2)}$  [Eq. (5)]. In total, we train 1166 parameters (360 coefficients for the radial functions and 403 coefficients each for  $\varphi_i^{(1)}$  and  $\varphi_i^{(2)}$ ). A single-shot fitting

TABLE II. Summary of the parametrization details used for the primary ACE potential developed in this work.

ACE details	Value
Energy expansion	FS type [Eq. (4)]
Cutoff	5.5 Å
Radial basis function	Spherical Bessel
$T$ order	1/2/3
$n_{\max}$	15/6/4
$l_{\max}$	0/3/3
Number of parameters (radial part)	360
Number of parameters $c_v^{(1)}$	403
Number of parameters $c_v^{(2)}$	403
Total number of parameters	1166

to the training data is performed using the Broyden-Fletcher-Goldfarb-Shanno (BFGS) algorithm to obtain the parameters.

For the Discussion section, we also train a set of ACE potentials with different cutoffs, body order  $T$ , and  $n_{\max}$  values to study their impact on the solid and liquid properties. Such an analysis is performed to understand the computational cost that comes with choosing a stricter set of initial conditions for training the ACE potential. The details of these additional potentials are specified in Table VI in the Discussion section.

### D. Molecular dynamics simulations

All MD calculations in this work are performed using the LAMMPS code [44] with the Performant implementation of the atomic cluster expansion (PACE) library [34,42,43]. The simulations are done on single-crystal bulk supercells, periodic in all directions, unless otherwise specified. Time integration is performed using the velocity Verlet algorithm [45] with a time step of 0.5 fs. Temperature and pressure control is done using a Nose-Hoover thermostat [46] and using the Parrinello-Rahman method [47], respectively. Structures are visualized using the OVITO software package [48]. Specific details regarding the MD runs are provided in the corresponding subsections in the Results section.

## III. RESULTS

### A. Fitting results

The root mean square errors (RMSE) and the mean absolute errors (MAE) of the fitted ACE on both the training set and the validation set are provided in Table III. As mentioned earlier, the validation set contains snapshots from the final 1000 steps of each AIMD calculation. The ACE potential

TABLE III. Summary of the fitting results. The chosen cutoff is 5.5 Å, with up to four-body interactions and  $n_{\max} = 15$  for  $T$  order = 1 as the initial specifications of the ACE potential. The validation set includes the final 1000 steps of each AIMD run.

	Energy (meV/atom)		Force (meV/Å)	
	Training	Validation	Training	Validation
RMSE	1.81	1.64	11.8	13.17
MAE	0.79	0.82	6.38	6.17

TABLE IV. Properties of Li at 0 K in the different energetically competing phases. Current DFT results and ACE predictions are compared to results from the literature. The table compares lattice constants  $a$  and  $c$  (in Å), equilibrium volume (in Å<sup>3</sup>/atom), cohesive energy  $E_{\text{coh}}$ , the energy difference with the fcc phase  $E - E_{\text{fcc}}$  (in eV/atom), and the elastic constants  $C_{ij}$  (in GPa).

Structure	Property	DFT (This work)	DFT/Expt. (Literature)	ACE (This work)	MEAM (Literature) <sup>b,d</sup>
fcc	$a$	4.331	4.324 <sup>a</sup> , 4.33 <sup>b</sup>	4.33	4.347, 4.298
	Volume	20.3097	20.211 <sup>a</sup> , 20.295 <sup>b</sup>	20.295	20.536, 19.849
	$E_{\text{coh}}$	-1.61	-1.611 <sup>b</sup>	-1.614	-1.63, -1.64
	$C_{11}$	16.4	16.2 <sup>c</sup>	17.1	16.02, 13.45
	$C_{12}$	12.5	12.5 <sup>c</sup>	13.1	12.13, 15.09
	$C_{44}$	10.1	10.4 <sup>c</sup>	12.1	10.92, 10.61
bcc	$a$	3.439	3.438 <sup>d</sup> , 3.51 <sup>e</sup>	3.438	3.451, 3.419
	Volume	20.336	20.318 <sup>d</sup> , 21.62 <sup>e</sup>	20.318	20.55, 19.983
	$E - E_{\text{fcc}}$	0.0016	0.0015 <sup>b</sup>	0.0036	0.00054, 0.0015
	$C_{11}$	14.6	15.0 <sup>f</sup>	15.0	16.7, 16.2
	$C_{12}$	13.7	13.2 <sup>f</sup>	13.4	12.6, 13.5
	$C_{44}$	11.5	11.1 <sup>f</sup>	10.9	11.2, 8.6
hcp	$a$	3.061	3.058 <sup>a</sup>	3.06	3.075, 3.033
	$c$	5.009	5.013 <sup>a</sup>	5.00	5.01, 5.015
	Volume	20.3225	20.298 <sup>a</sup>	20.3	20.512, 19.976
	$E - E_{\text{fcc}}$	0.00019	0.0001 <sup>d</sup>	0.0003	0.0005, 0.00074
	$C_{11}$	26.6	22 <sup>f</sup>	24.1	21.1, 14.1
	$C_{12}$	10.9	11 <sup>f</sup>	10.9	12.8, 22.2
	$C_{13}$	5.2	8 <sup>f</sup>	5.1	6.3, 6.4
	$C_{33}$	32.1	26 <sup>f</sup>	31.3	27.6
	$C_{44}$	7.9	6 <sup>f</sup>	7.7	4.4, 2.8
h9R	$a$	3.06	3.08 <sup>g</sup>	3.04	
	$c$	22.53	22.37 <sup>g</sup>	22.3	
	Volume	20.313	20.42 <sup>g</sup>	20.1	
	$E - E_{\text{fcc}}$	0.00014	0.000	-0.0001	
	$C_{11}$	19.1	19 <sup>g</sup>	20.24	
	$C_{12}$	13.6	14 <sup>g</sup>	14.4	
	$C_{13}$	7.5	8 <sup>g</sup>	6.9	
	$C_{33}$	27.1	27 <sup>g</sup>	24.3	
	$C_{44}$	6.3	5 <sup>g</sup>	7.4	
	$C_{66}$	1.8	2 <sup>g</sup>	2.1	
	$C_{14}$	1.1	1 <sup>g</sup>	1.6	

<sup>a</sup>Reference [51]; <sup>b</sup>Reference [12]; <sup>c</sup>Reference [7]; <sup>d</sup>Reference [11]; <sup>e</sup>Reference [52]; <sup>f</sup>Reference [53]; <sup>g</sup>Reference [54].

predicts extremely accurate values of the energies and forces of configurations from both the training and validation sets: errors below 2 meV/atom for energies and 14 meV/Å for forces. Below, we further use the ACE potential to predict 0 K and high-temperature properties of solid and liquid Li.

## B. Solid lithium

### 1. 0 K phases

The 0 K properties predicted by the ACE potential are compared to corresponding DFT or experimental data and results from the literature obtained using previously existing 2NN-MEAM interatomic potentials for solid Li [11,12]. In Table IV we provide an extensive set of such properties for the fcc, bcc, hcp, and h9R phases. Here, we have also compared the DFT results obtained in this work which are calculated as a part of the training set generation. The properties of the h9R phase were not calculated in the literature of the previously existing potentials and are hence left blank.

From the DFT results in Table IV it is seen that the fcc phase is the lowest-energy ground state structure at 0 K, which has been previously established in the literature [7]. The bcc, hcp, and h9R are metastable phases, but energetically very close to the fcc phase as noticeable from the energy differences. The ACE potential also predicts the fcc phase to have a lower energy than the bcc and hcp phases, though the energy difference between the bcc and fcc phases is marginally higher (by 0.002 eV/atom) than for DFT. However, the ACE potential predicts the h9R phase to be lower in energy than the fcc phase by 0.0001 eV/atom. In addition to the energy differences, the elastic constants predicted by the ACE potential are also in good agreement with DFT for all phases and each of them satisfies the Born criteria [49]. The positive values of  $C' = C_{11} - C_{12}$  also indicate that there is no spontaneous fcc-bcc Bain transformation. Rather, the transformation happens through an intermediate high-energy mean-centered cubic phase as discussed in Ref. [50]. Overall, the ACE property predictions of the different phases are very

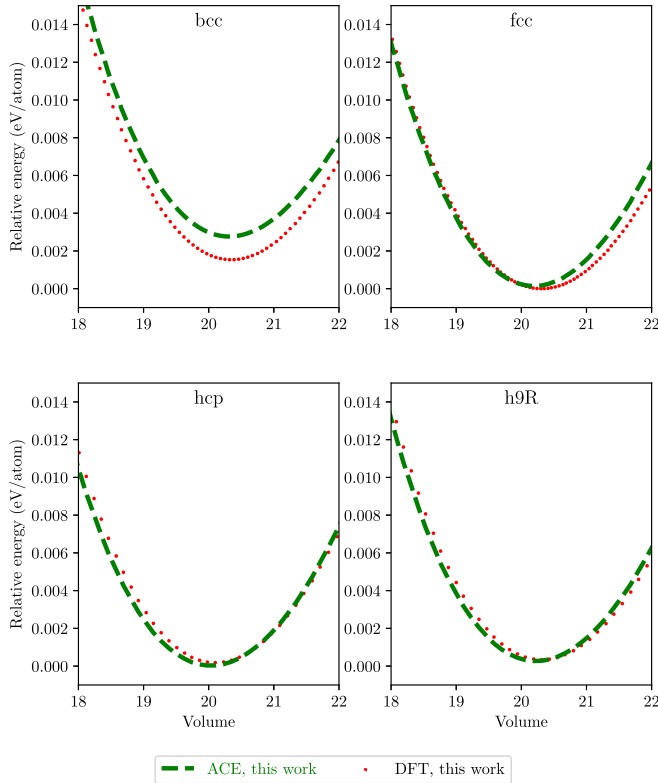


FIG. 1. Energy-volume curves of the four phases with respect to the equilibrium 0 K fcc energy predicted by the ACE potential compared to DFT.

satisfying, considering the extremely small energy differences between the different phases. Nonetheless, the bcc phase is known to become entropically stabilized above  $\approx 100$  K.

The 0 K energy-volume curve predicted by the ACE potential is compared to the DFT results for four phases in Fig. 1. Here, the energies are with respect to the equilibrium fcc energy. The hcp and h9R energies are almost exactly reproduced, while our ACE potential predicts a marginally higher energy for the bcc phase by less than 0.002 eV/atom. The ACE also predicts the bcc phase to be slightly softer which is noticeable from the small difference in curvature of the energy-volume plot. This difference might arise from the fact that there are several high-temperature bcc configurations in the training set. The elastic constants and bulk modulus are lower at a higher temperature, driving the ACE potential towards predicting a slightly softer bcc phase even at 0 K.

## 2. Vacancies and self-interstitial defects

In addition to the 0 K energies and phase stabilities discussed above, we also validate the 0 K defect and surface energies predicted by the ACE potential. We restrict these comparisons only to the experimentally observed bcc phase. Table V shows the formation energies of a mono-, di-, and trivacancy, five self-interstitial defects, and three different surface energies. The formation energies of vacancies and SIA defects are calculated as  $E^{\text{formation}} = [E_{\text{with defect}} - (N_{\text{with defect}}/N) \times E_{\text{bulk}}]$ . The table also compares the total binding energies of the di- and trivacancy, which are calculated as

TABLE V. Comparison of certain vacancy formation, vacancy binding, self-interstitial formation, and surface energies of bcc Li predicted by the ACE potential to DFT.

Property	Type	DFT (This work)	ACE (This work)
Vacancy formation energy (eV/atom)	Monovac	0.457	0.437
	Divac	0.952	0.92
	Trivac	1.397	1.41
Binding energy (eV/atom)	Divac	-0.038	-0.04
	Trivac	-0.026	-0.014
Self-interstitial formation energy (eV/atom)	$\langle 111 \rangle$	0.527	0.511
	$\langle 110 \rangle$	0.617	0.58
	$\langle 100 \rangle$	0.757	0.689
	Octahedral	0.81	0.77
	Tetrahedral	0.834	0.813
Surface energy (eV/Å <sup>2</sup> )	{110}	0.029	0.022
	{100}	0.027	0.023
	{111}	0.041	0.046

$E^{\text{binding}} = (n \times E_{\text{monovac}}^{\text{formation}} - E_{\text{di/trivac}}^{\text{formation}})$  with  $n$  equal to 2 or 3 for the di- and trivacancy. The surface energy is calculated as  $E^{\text{surface}} = (E_{\text{with surface}} - E_{\text{bulk}})/(2 \times \text{Area})$  using a large simulation box with a free surface on either side of the axis and periodic along other dimensions. The ACE potential predicts defect energies in very good agreement with DFT. In solid bcc Li, the binding energy of di- and trivacancies is negative, suggesting that there is no inclination towards the formation of vacancy clusters, as predicted both by DFT and the ACE potential. The ACE potential and DFT both predict the  $\langle 111 \rangle$  self-interstitial to be the lowest-energy interstitial defect in bcc Li. Similarly, both the ACE potential and DFT predict the {100} and {110} surfaces to be the lowest-energy surfaces, though the ACE potential predicts the {110} to be lower in energy than the {100} surface by only 0.001 eV/atom.

## 3. Temperature dependent properties

Next, we also use the ACE potential to calculate temperature dependent properties of solid bcc Li. Figure 2 shows the change in lattice constant with temperature predicted by the ACE potential, in comparison to experiments reported in the literature. The slope of the curve (related to the coefficient of thermal expansion) agrees with the experimental data, although the absolute values are slightly smaller (by around 0.02–0.04 Å). The smaller lattice constant predicted by the ACE potential in comparison to the experiment value is also observed at 0 K (3.438 Å versus 3.51 Å; refer to Table IV). The smaller lattice constant predicted by the ACE potential is a consequence of training it on energies and forces calculated using the GGA exchange-correlation functional. The GGA functional already predicts an overbinding solid with a smaller lattice constant than experiments (3.439 Å versus 3.51 Å at 0 K; refer to Table IV). The overbinding nature of the GGA functional has been observed in the literature for many transition metals [55]. Hence, since the ACE potential is trained on overbinding GGA functional values, it also predicts overbinding of solid Li, leading to slightly smaller values of

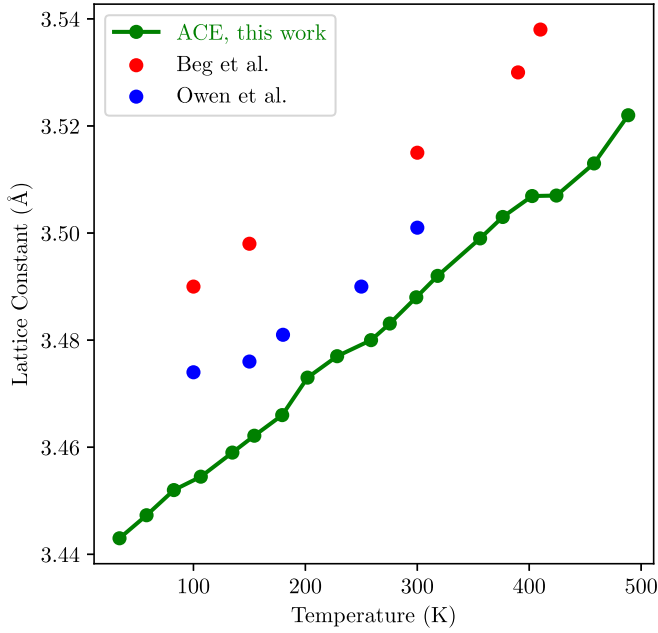


FIG. 2. Lattice constant as a function of temperature for the bcc phase predicted by the ACE potential compared to experimental values [56,57].

lattice constant compared to experimentally measured values, both at 0 K and finite temperature.

In Fig. 3, we plot the change in elastic constants ( $C_{11}$ ,  $C_{12}$ , and  $C_{44}$ ) of the bcc phase predicted by the ACE potential compared to experimental data from the literature. The slope of the curves are consistent and the absolute values are accurately predicted by the ACE potential. All three elastic constants decrease by 3–4 GPa from 0 K to 400 K, making the bcc solid softer with increasing temperature. The  $C'$  values are positive at all temperatures for bcc Li.

#### 4. Effect of stress on bcc Li

To study the effect of stress on bcc Li at room temperature using the ACE potential, we perform MD simulations of strain-controlled tensile and compressive loading. Following

thermal equilibration at 300 K for 20 ps, the loading is performed at a rate of  $0.3 \text{ fs}^{-1}$  up to 10% strain. Zero stress is applied in the directions perpendicular to the direction of the applied strain, allowing the sample to change shape in those directions.

Figure 4(a) shows the stress-strain behavior during two such loading scenarios—compressive loading along the  $\langle 100 \rangle$  direction and tensile loading along the  $\langle 110 \rangle$  direction. Initially, the bcc phase strains elastically with an orientation-dependent Young's modulus. Based on the Bain transformation, one would expect the bcc phase to transform into the fcc phase at higher strains. However, there is a large strain mismatch between the fcc and bcc phases that is dependent on the loading direction. The MD simulations reveal that bcc Li instead transforms into a disordered stack of fcc-type and hcp-type sequences as shown in Figs. 4(b) and 4(c), for the case of compressive strain along  $\langle 100 \rangle$  and tensile strain along  $\langle 110 \rangle$ , respectively. The transformation begins at strains corresponding to points A and B in Fig. 4(a) and continues up to points C and D, after which the stacked structure starts elastic deformation. The fcc-hcp stacks created during the phase transformation are formed on  $[110]$  planes. Given that the fcc and hcp phases are energetically very close (refer to Table IV), and to avoid high stresses at larger strains, the bcc structure transforms into a stacked fcc-hcp structure rather than a perfect fcc one along these orientations. The thickness of the fcc and hcp layers that are formed under strain-controlled loading is dependent on the loading direction and we restrict the results to the above-discussed two conditions. The observation of such close-packed fcc-hcp stacking structures in both experiments and MD simulations is discussed further in the Discussion section.

### C. Liquid lithium

#### 1. Melting point prediction

The ACE potential, which is trained on solid and liquid configurations, is also used to predict the melting point of Li. In this work, we use the solid-liquid coexistence method [61] to compute the melting point. The MD calculation is performed in a 55 296-atom simulation cell

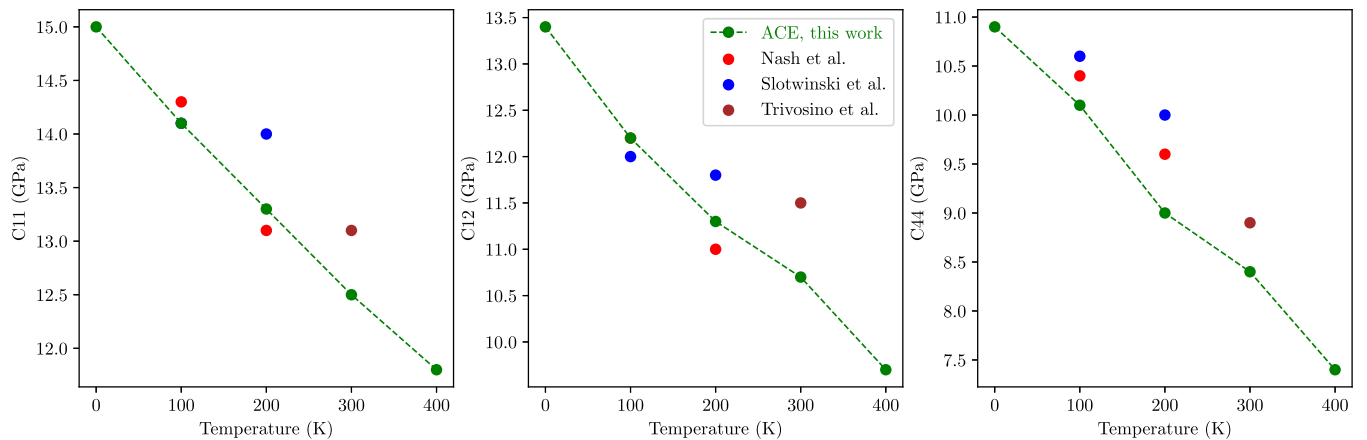


FIG. 3. Elastic constants as a function of temperature for the bcc phase predicted by the ACE potential compared to experimental values [58–60].

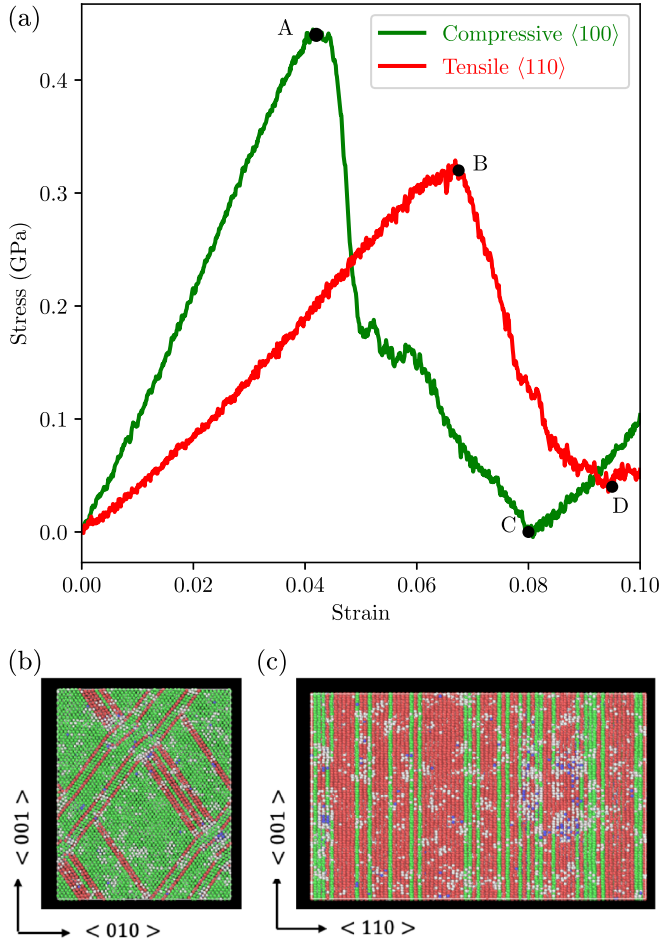


FIG. 4. (a) Stress-strain behavior of bcc Li at 300 K when loaded in compression along the  $\langle 100 \rangle$  direction (green) and in tension along the  $\langle 110 \rangle$  direction (red). The bcc phase starts phase transforming at points A and B, respectively. Atoms are visualized at the end of the transformation (corresponding to points C and D) in figures (b) and (c), respectively. The atoms are colored according to the common neighbor analysis: green is fcc, pink is hcp, blue is bcc, and white is other structure types.

(8.3 nm  $\times$  8.3 nm  $\times$  16.5 nm), divided equally into two parts. Initially we fill the cell with perfect bcc Li and perform an energy minimization of the entire cell. We then thermally equilibrate the whole system at the speculated melting point ( $T_{\text{guess}}$ ) for 50 ps: conventionally, we can use the experimental melting point of Li as the initial guess. Next the bottom half of the simulation cell is kept frozen and the top half is heated from  $T_{\text{guess}}$  to  $2 \times T_{\text{guess}}$  in an *NPT* ensemble over 60 ps, with the cell allowed to relax perpendicular to the plane of separation of the frozen and unfrozen atoms ( $z$  axis). The above step melts the top half of the cell. We proceed to cool the top half, again in a similar *NPT* ensemble, from  $2 \times T_{\text{guess}}$  back to  $T_{\text{guess}}$  in 60 ps, which still keeps the top half of the cell melted. As the final step, we release all atoms by relaxing the entire system in an *NPH* ensemble for 0.5 ns. If the initial guess is close to the predicted melting point, then the system reaches a steady temperature while still maintaining an approximately 50-50 ratio of the solid and liquid phases in coexistence. That temperature is the melting point of the system as predicted by

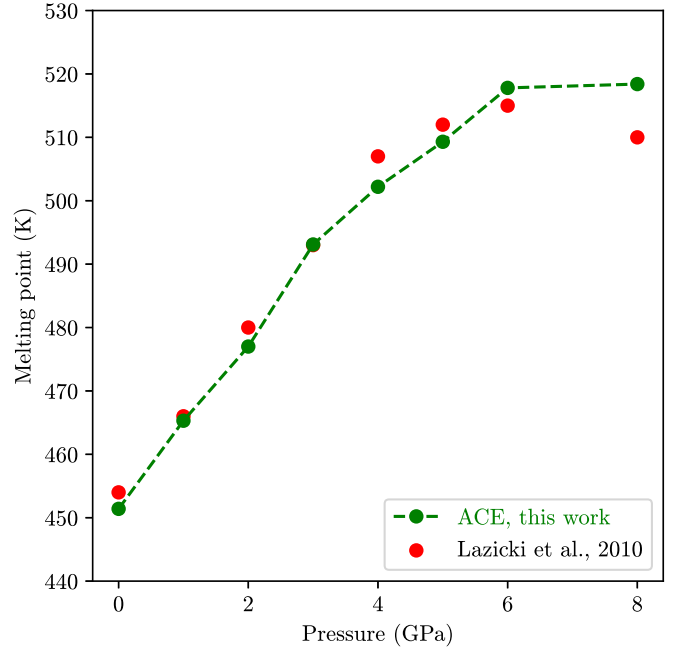


FIG. 5. Change in the melting point predicted by the ACE potential as a function of pressure compared to experimental values [62].

the ACE potential. If the initial guess is too high, the entire system melts in the final step; if it is too low the whole system freezes. Accordingly,  $T_{\text{guess}}$  is altered for the next simulation trial and the process continues until the melting point is estimated. The melting point can be calculated as a function of pressure by following the above procedure, but maintaining the corresponding pressure in the *NPT* and *NPH* ensembles.

Figure 5 shows the estimated melting point as a function of pressure predicted by the ACE potential compared with experimental data from the literature [62]. The zero-pressure melting point is predicted to be 451 K, very close to the experimental value of 454 K. The ACE potential also replicates the increase and eventual levelling off of the melting point as a function of pressure. The estimated values are higher than experiment by less than 10 K at a pressure of around 8 GPa. We expect this discrepancy to arise for one of two reasons. The bcc phase transforms into the fcc phase around 8–10 GPa [4], further complicating the solid-liquid phase diagram at those pressures: this might be a source of the error in the ACE prediction. We also noticed a significant improvement in the predicted melting point at high pressures when corresponding high-pressure bcc DFT structures were added to the training data (notice the additional volume for bcc AIMD in Table I). Hence another source of this error might be that there is still insufficient training data corresponding to the bcc-fcc-liquid triple point.

## 2. Liquid properties

The results shown for liquid Li have been averaged over MD simulations performed with five different initial liquid structures with different initial random velocity seeds. Each MD run is performed on a 27 648-atom (8.3 nm  $\times$  8.3 nm  $\times$  8.3 nm) simulation cell. The liquid structures are created by performing a thermal equilibration at the corresponding

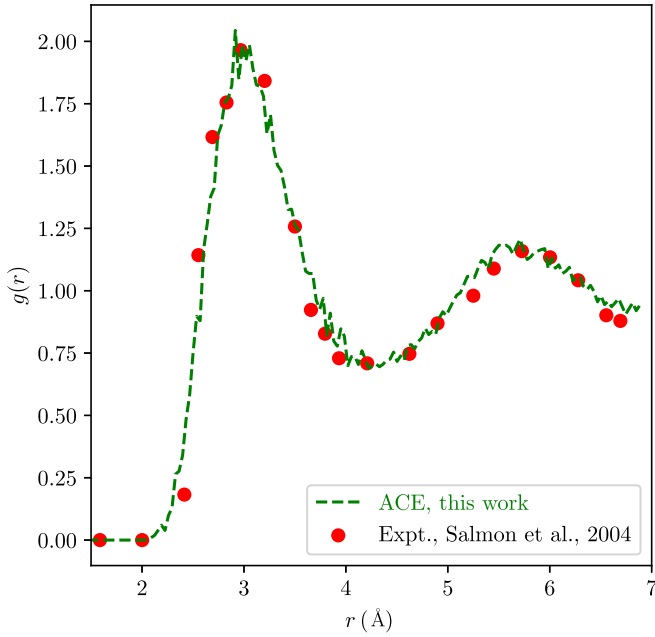


FIG. 6. Radial distribution function for liquid Li at 868 K compared to experimental values from the literature [63].

temperature for 50 ps. Figure 6 shows the radial distribution function (RDF) of liquid Li at 868 K predicted by the ACE potential. The ACE potential results agree very well with the experimental data from the literature [63]. As expected for a liquid structure, the RDF is broadened relative to the solid, with two broad peaks with maxima close to 3 Å and 5.8 Å.

Figure 7 shows the shear viscosity of liquid Li calculated at different temperatures using the ACE potential and compared

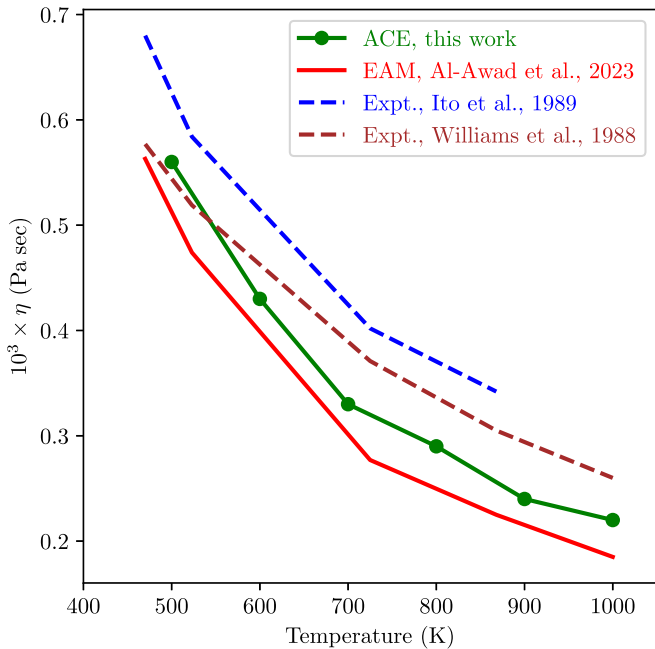


FIG. 7. Shear viscosity of liquid Li predicted by the ACE potential at volumes corresponding to that temperature in comparison to EAM and experimental data from literature [18,64,65].

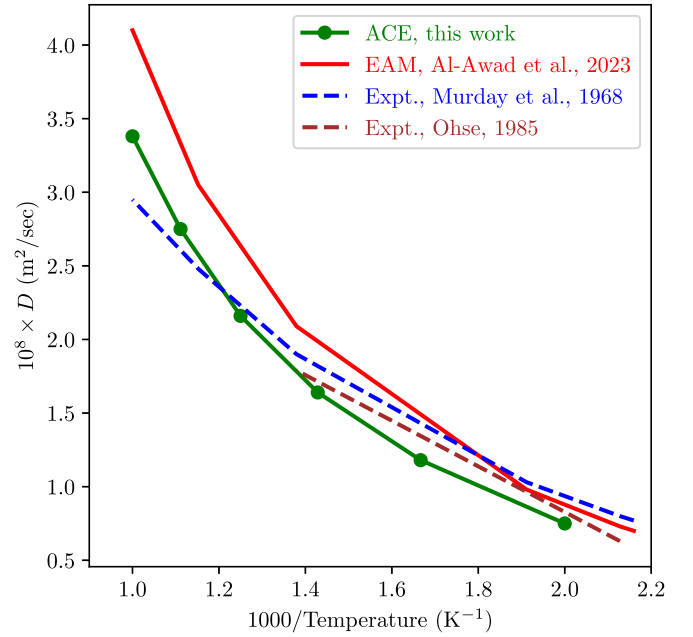


FIG. 8. Self-diffusion coefficient of liquid Li predicted by the ACE potential at volumes corresponding to that temperature in comparison to EAM and experimental data from literature [18,66,67].

to experimental values. The shear viscosity  $\eta$  is calculated using the Green-Kubo formalism and is given by

$$\eta = \frac{V}{k_B T} \int_0^\infty dt \langle \tau_{\alpha\beta}(t) \tau_{\alpha\beta}(0) \rangle_{t_0}, \quad (10)$$

where  $V$  is the system volume,  $k_B$  is the Boltzmann constant,  $T$  is the temperature,  $\tau_{\alpha\beta}$  are off-diagonal components of the stress tensor,  $t$  is the time, and  $\langle \dots \rangle_{t_0}$  is the average over time origins. Following the aforementioned 50 ps thermal equilibration, time window averages are taken every 1 ps, by considering input values every 2.5 fs and accumulating 400 correlation time windows. The predictions [18] of a previously developed EAM for liquid Li are also plotted in Fig. 7 for comparison. The ACE potential predicts a considerable drop in the shear viscosity of liquid Li with increasing temperature, which is also observed experimentally. The absolute values of the viscosity from the ACE potential are closer to experiment than the predictions of the EAM potential.

The next liquid Li property that we predict and compare is the self-diffusion coefficient  $D$ , which is calculated from the mean-squared displacement (MSD) and is given by

$$D = \frac{1}{6t} \langle [r(t) - r(0)]^2 \rangle, \quad (11)$$

where  $r(t)$  is the position of an atom at time  $t$ . To obtain the MSD we first performed a thermal equilibration for 1 ns at the corresponding temperature in an  $NPT$  ensemble. A straight line is then fitted to the MSD as a function of time for the final 0.8 ns of the simulation in order to obtain the self-diffusion coefficient. The self-diffusion coefficients calculated at different temperatures using the ACE potential are plotted in Fig. 8. The values and the trend of the self-diffusion coefficient obtained from the ACE potential are close to experimental values. For

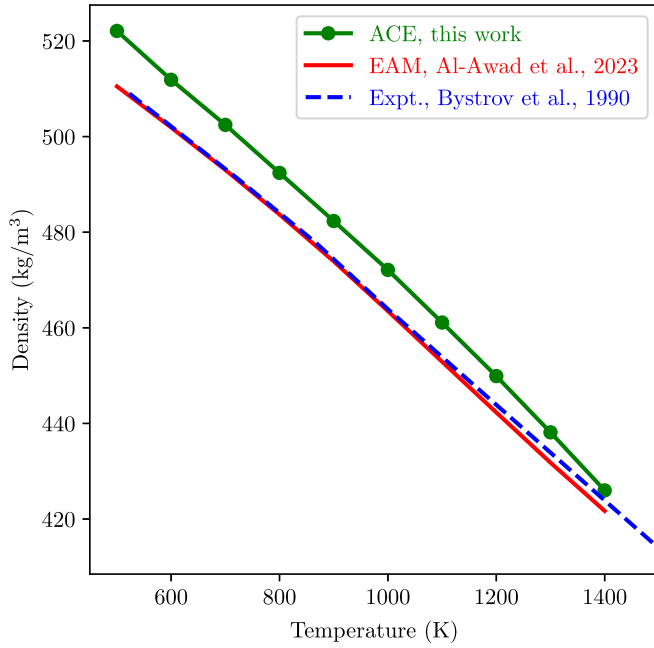


FIG. 9. Density of liquid Li at 1 atmospheric pressure as a function of temperature predicted by the ACE potential in comparison to EAM and experimental data from literature [18,68].

comparison, the EAM-predicted values are also plotted in the same figure.

In Fig. 9 we plot the liquid density as a function of temperature as predicted by the ACE potential. The densities are also obtained from the MD runs mentioned in the earlier paragraph. We average the volumes during the last 0.8 ns of the run to obtain the density at the corresponding temperature. The ACE-predicted density is compared to experimental values [68] and values predicted using an EAM potential [18]. The densities predicted by the ACE potential are marginally higher than the experimental values by around 5–15 kg/m<sup>3</sup>. This can again be attributed to the effect of the overbinding from the GGA exchange and correlation functional to which the ACE potential is trained. On the other hand, the EAM potential was trained on experimental values of the density, which is why the EAM prediction falls exactly on top of the experimental curve. Nonetheless, this does not get translated to other liquid properties that were discussed earlier, where the predictions of the ACE potential were closer to experimental values. Overall, while the EAM potential shows a decent performance when predicting liquid properties, the ACE potential performs better. The ACE potential also simultaneously predicts solid Li and the melting points accurately and provides a platform for studying more complex systems containing liquid lithium.

Since we have established the accuracy and predictive capability of the ACE potential, we use it to calculate the pressure-volume (PV) isotherms for liquid Li as shown in Fig. 10. The liquid Li structure is thermally equilibrated at the corresponding temperature and pressure in an *NPT* ensemble for 100 ps. The volume is calculated as an average during the second half (final 50 ps) of the simulation. Li stays in the liquid phase even up to higher pressures of 12 GPa. The thermal expansion coefficient of liquid Li, reflected in the

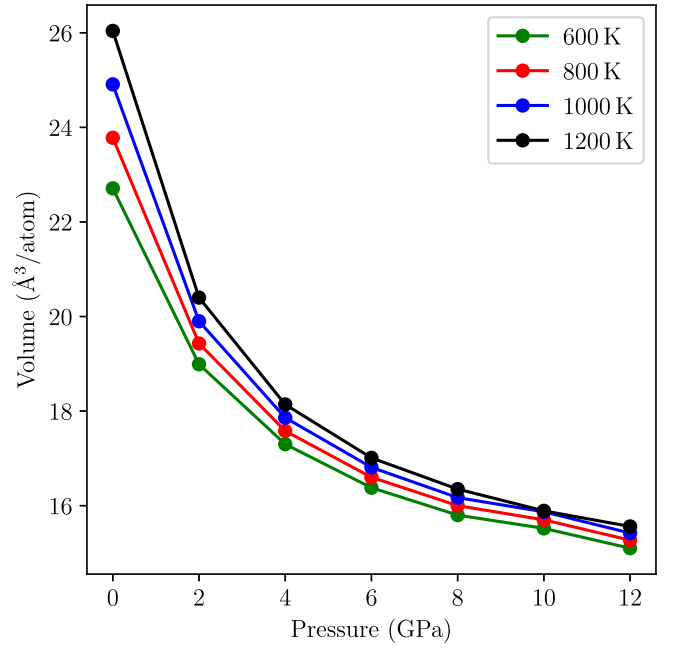


FIG. 10. Pressure-volume isotherms for liquid Li calculated using the ACE potential.

change in volume with temperature, decreases with increasing pressure. The isotherms provide an accurate estimate of the volume of liquid Li for high-pressure applications.

#### IV. DISCUSSION

So far, in this work, we developed an ACE interatomic potential to predict both solid and liquid Li properties. We performed MD simulations using the ACE potential to predict finite-temperature properties of both phases. At room temperature, solid bcc Li underwent a martensitic phase transformation under the application of a uniaxial strain. A compressive strain along  $\langle 100 \rangle$  or a tensile strain along  $\langle 110 \rangle$  formed fcc-hcp stacking sequences due to the large strain mismatch between the bcc and fcc phase. The thickness of the stacks varied with different loading directions. Similar disordered polytype structures have been reported experimentally under different external conditions [69–72] and in MD simulations during cooling of the bcc phase using the MEAM potential [11]. The ACE potential lets us predict the orientation-dependent onset of such structures also under different loading scenarios. Understanding such behavior under the application of an external load will be crucial in the design and manufacture of solid Li-based materials.

MD simulations using the potential were also performed to obtain several crucial properties of liquid Li at different temperatures. Specifically, we obtained accurate predictions of the temperature-dependent viscosity and self-diffusion, and the pressure-volume isotherms, which will in turn feed into larger-scale modeling of liquid flow in Li. With Li being considered as a potential candidate for cooling channels in breeder blankets, accurate modeling of the liquid flow is essential in optimizing the design of such coolants.

The ACE potential that we developed so far included up to four-body interactions with  $n_{\max} = 15$  in the expansion

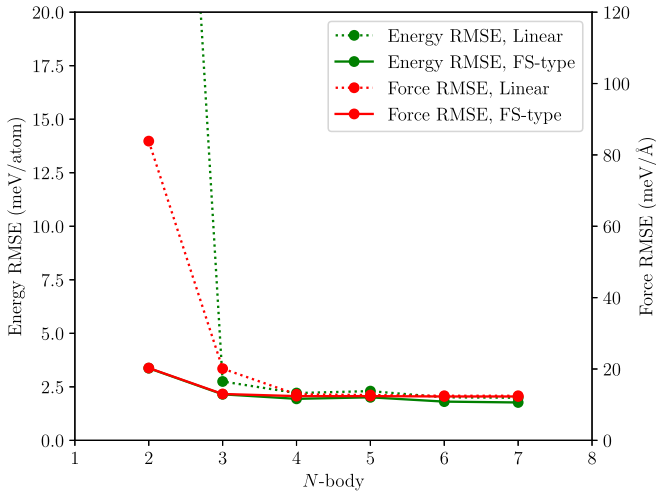


FIG. 11. Root mean squared errors (RMSE) in the energy and atomic forces as a function of the  $N$ -body interactions considered in the ACE model. Linear and Finnis-Sinclair type of energy expansion of the ACE formalism are compared.

of the radial basis and we imposed a  $5.5 \text{ \AA}$  cutoff on the interatomic interactions in the training set. The performance of the potential was exceptional in predicting both the solid and liquid phase properties and the melting point in comparison to *ab initio* values. Indeed, some of the observed errors are from the underlying DFT data rather than the model itself. However, owing to the large parameter space, the developed potential is roughly two orders of magnitude slower than classical interatomic potentials. Nonetheless, one of the advantages of the ACE formalism is to systematically investigate the effect of higher-body interactions in a model system—in our case, lithium. Since the number of basis functions, and consequently the cost of performing MD simulations, become higher with the inclusion of higher body interactions, it is crucial to find an optimally performing ACE potential for lithium in terms of both computational cost and accuracy.

Figure 11 shows the RMSE in energies and forces during training of various lithium ACE potentials that included increasing orders for the  $N$ -body interactions in the ACE basis [Eq. (8)]. The change in the RMSE is shown for ACE potentials of both the linear type [Eq. (3)] and the nonlinear Finnis-Sinclair type [Eq. (4)]. It is observed that the FS-type ACE potential (shown as solid lines in Fig. 11) converges faster in terms of the RMSE than the linear type. Indeed, the FS-type ACE potential is already well converged after including only up to three-body interactions. This implies that almost all interactions in lithium can be represented by considering only the two-body and three-body interactions to the atomic energy, provided we expand the energy as a sum of a linear term that signifies pairwise forces and a square root term that signifies the embedding function. This might explain the success of the MEAM potential. However, if the formalism does not include an explicit embedding-type term, one also needs to consider four-body interactions before reaching a converged error in the trained energies and forces. The faster convergence of the FS-type formalism can be partially explained by its larger parameter space in comparison to the

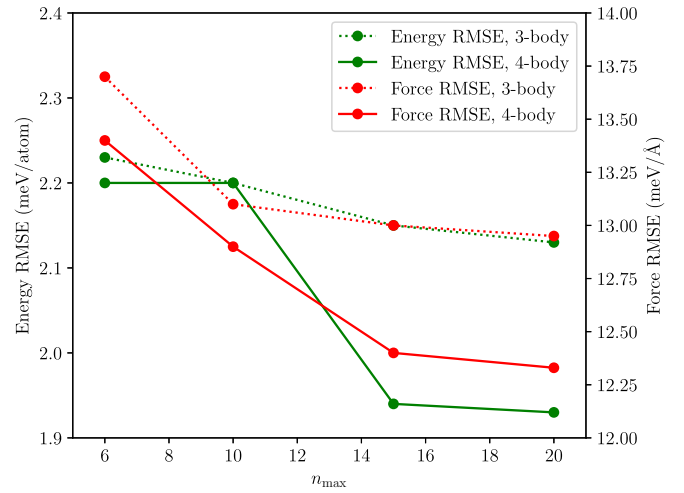


FIG. 12. Root mean squared errors (RMSE) in the energy and forces as a function of  $n_{\max}$  that is used in the expansion of the radial basis for the three-body and four-body interaction ACE models, FS-type formalism only.

linear-type for the same  $N$ -body contributions and training data, as two functions need to be learned rather than just one.

In Fig. 12, we show the RMSE in energies and forces of various ACE potentials as a function of  $n_{\max}$  in the expansion of the radial function [Eq. (6)]. The value of  $n_{\max}$  corresponds to the value of  $n$  for the two-body interaction term. The other values of  $n$  and  $l$  are those given in Table II. The RMSEs are shown only for the FS-type formalism while including up to three-body and four-body interaction terms in the expansion. The RMSE values converge after a value of  $n_{\max} = 15$ . However, the errors are already very small with just six terms in the expansion of the radial function. The gain in accuracy is not very significant when going from  $n = 6$  to  $n = 15$  and there is a considerable rise in the computational cost (check Table VI) as will be discussed later.

The other parameter in the ACE formalism that affects the performance and computational cost is the cutoff chosen for the interatomic interactions. While a larger cutoff implies a greater accuracy in the atomic energy in the training data, it also implies a larger number of energy and force calculations per atom per MD step with the trained potential, which increases the computational cost. Figure 13 shows the RMSE in energies and forces of ACE potentials fitted with different cutoffs. In the figure, we only show the case for FS-type ACE potentials including up to four-body interactions with  $n_{\max} = 15$ . The errors are extremely small (less than 2 meV in energy and 13 meV  $\text{\AA}$  in atomic forces) for a  $5.5 \text{ \AA}$  cutoff and become even smaller and converge to below 0.1 meV in energy at a  $7 \text{ \AA}$  cutoff, albeit at a higher computational cost (see below and Fig. 14).

The above analysis reveals that the RMSE in energy and atomic forces of a trained ACE potential converge to within 2 meV/atom and 15 meV/ $\text{\AA}$  compared with *ab initio* values as long as we choose a nonlinear formalism of the ACE potential that includes up to four-body interactions, with an  $n_{\max}$  value of 15 to expand the radial basis and a cutoff of  $5.5 \text{ \AA}$ . In fact, to obtain an ACE potential to predict properties of only the

TABLE VI. Comparison of the energy differences of different competing phases in solid Li (in eV) and the 0 K bcc and fcc elastic constants (in GPa) as predicted by ACE potentials fitted with different initial conditions to DFT (last line). In the last two columns, the fitting time and usage time of the potentials are compared. The time to fit is measured after 1000 iterations on a single node with 48 CPUs. The usage time is measured as the number of LAMMPS MD steps per second on a 16 384 atom system on a single node with 48 CPUs.

ACE parameters	$\Delta E_{\text{bcc-fcc}}$	$\Delta E_{\text{hcp-fcc}}$	$\Delta E_{\text{h9R-fcc}}$	Elastic constants bcc			Elastic constants fcc			Time to fit (s)	Usage (steps/s)
				$C_{11}$	$C_{12}$	$C_{44}$	$C_{11}$	$C_{12}$	$C_{44}$		
Two-body, 5.5 Å, $n = 15$	0.007	0.0064	0.0015	11.1	12.8	9.9	19.4	13.3	12.1	4180	247
Three-body, 5.5 Å, $n = 15$	0.0045	0.0032	0.0029	11.9	12.1	10.9	18.8	13.5	10.9	6558	58
Four-body, 5.5 Å, $n = 6$	0.0053	0.0029	0.0022	12.0	12.2	9.7	17.9	11.1	10.1	5099	81
Four-body, 5.5 Å, $n = 10$	0.005	0.0033	0.002	12.8	13.1	11.0	17.1	13.4	12.2	6180	69
Four-body, 5.5 Å, $n = 15$	0.0036	0.0003	-0.0001	15	13.4	10.9	17.1	13.1	12.1	7019	33
Four-body, 7 Å, $n = 15$	0.0026	0.00013	0.0009	15.1	13.9	10.9	16.9	13.1	10.2	8800	21
Five-body, 5.5 Å, $n = 15$	0.0034	0.0018	0.0009	13.8	13.1	10.2	16.4	14.7	10.8	7937	27
Six-body, 5.5 Å, $n = 15$	0.0035	0.0018	0.0008	13.9	13.2	10.3	16.3	14.5	10.8	10898	22
DFT	0.0016	0.00019	0.00014	14.6	13.7	11.5	16.4	12.5	10.1		

liquid phase by training on *ab initio* MD data of liquid Li (last row in Table I), expanding the energy to include as much as up to three-body interactions is sufficient to obtain converged properties of the liquid phase. This has been further discussed in the Supplemental Material D [31].

Including higher body terms is crucial primarily in obtaining the correct 0 K energy differences of the different competing solid phases and the elastic constants of the bcc and the fcc solid. This is evident from Table VI, which compares these properties for ACE potentials that were trained with different sets of input conditions to the same DFT training data. Including four-body interaction terms and choosing a larger  $n_{\text{max}}$  brings the energy difference between the bcc, hcp, and the h9r phases and the fcc phase much closer to the DFT values. A stricter set of parameters is also necessary for obtaining accurate values of the 0 K elastic constants and especially the correct order of elastic constants (with  $C_{11} > C_{12}$ ) for the bcc phase that satisfies the Born criterion. A significant gain in accuracy is not observed by increasing the cutoff to 7 Å.

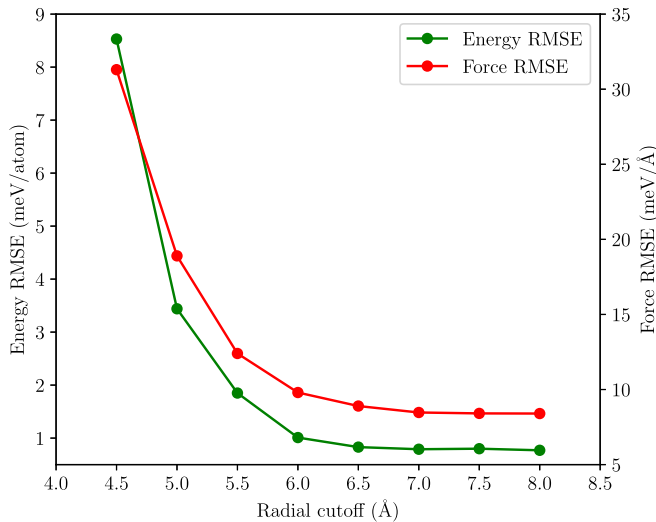


FIG. 13. Root mean squared errors (RMSE) in the energy and forces as a function of the radial cutoff for FS-type ACE potentials with  $n_{\text{max}} = 15$  and up to four-body interactions.

Similarly, adding higher body-order interaction terms above 4 does not further improve the predictions of the ACE potential.

Although considering a higher set of input parameters (body order,  $n_{\text{max}}$ , and cutoff) brings the ACE predictions much closer to DFT, this also significantly increases the computational cost, both for fitting and, more importantly, for running MD simulations with the fitted potential. The increase in computational cost for different initial conditions is compared in the last two columns in Table VI. The values are also plotted in Fig. 14 for two specific cases that compare the fitting time and the utility (number of MD steps that can be run per second) as a function of the body order for ACE potentials trained with 5.5 Å and 7 Å cutoffs. Both the fitting time and the usage time are a function of the total number of parameters in the ACE potential. The fitting time steadily increases with increase in the body order. By considering an expansion with more than three-body interaction terms, there is a steady

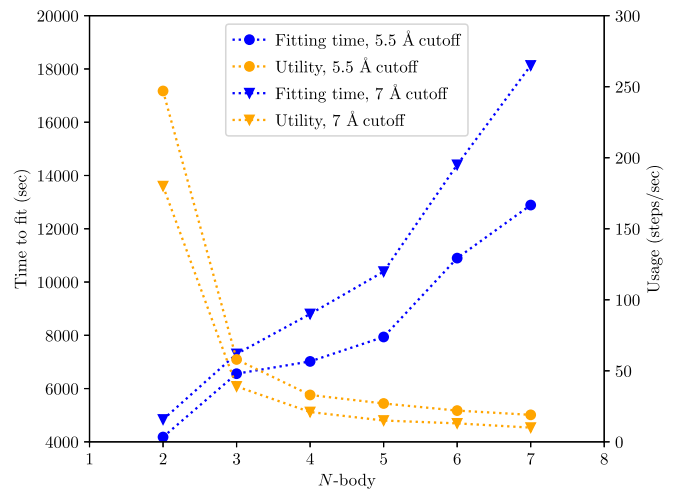


FIG. 14. Time required to fit and the computational cost of doing MD using the ACE as a function of  $N$ -body interactions used in the ACE model. The fitting time is measured after 1000 iterations on a single node with 48 CPUs. The usage time is measured as the number of MD steps per second on a 16 384 atom system on a single node with 48 CPUs.

increase in the computational cost of the ACE potential. The ACE potentials trained with a 7 Å cutoff are roughly twice as expensive as the one with 5 Å. Overall, by performing such an analysis, we are able to make an informed decision about the level of the ACE potential that is needed to efficiently model a given system. It is left up to the discretion of the MD user to choose a corresponding ACE potential based on the accuracy and the computational cost that can be afforded. For the case of lithium, an ACE potential that predicts both the solid and liquid phases and melting properties accurately requires initial training specifications as mentioned in Table I, which have been shown to perform exceptionally in the Results section of this manuscript.

## V. CONCLUSIONS

In this work, we have developed an atomic cluster expansion interatomic potential for lithium. The potential predicts accurate properties of both the solid and liquid phases and an accurate melting point in comparison to 0 K DFT, finite-temperature *ab initio* data and experiments. Solid properties studied include lattice parameters, cohesive energies, elastic constants, and point defect formation energies. The effect of uniaxial strain and martensitic transformation in solid bcc Li is also modeled using MD simulations with the ACE potential. Liquid properties studied include melting point, radial distribution function, shear viscosity, and pressure-volume isotherms. We have performed an extensive cost-accuracy analysis by training several potentials using the ACE formalism. Most of the interactions in lithium can be captured by expanding the energy using three-body terms. Hence a relatively computationally cheaper three-body expanded ACE potential is sufficient to model liquid lithium. However, including four-body interactions in the ACE expansion is absolutely crucial in capturing the correct 0 K energies and elastic constants of different competing phases in solid Li. We note that the potential is able to reproduce the DFT data

sufficiently accurately that in some cases the underlying errors from the DFT exchange and correlation functional can be the largest source of error.

The ACE potential developed in this work can be used to study the effect of stress and temperature in polycrystalline solid Li to parametrize higher scale models. The potential will also be extended to include hydrogen interactions in the future to model lithium breeder blanket systems. Liquid Li has also been suggested as a candidate material for first walls and divertors [73] in nuclear fusion reactors. The potential will thus be fine-tuned and used to perform MD simulations of radiation damage and model sputtering from the surface of liquid Li. The results discussed in this work will also be useful to benchmark and analyze the performance of emerging universal MLIPs [74–77] for studying hydrogen diffusion in lithium and lithium-based compounds in the future.

## ACKNOWLEDGMENTS

This project was funded by UKAEA through the Department for Science, Innovation and Technology's International Science Partnership Fund (ISPF). D.N.M. and P.S. would like to thank the EUROfusion for providing Fusion HPC facilities on Marconi and Leonardo machines in generation of the DFT data used for this paper. P.S., M.R.G., and D.N.M. also acknowledge funding by the EPSRC Energy Programme (Grant No. EP/W006839/1). D.N.M., A.P.H., and P.S. would like to thank R. Drautz and M. Mrovec for their discussions regarding the ACE method. A.P.H., S.P., and K.P.D. would like to acknowledge the Imperial College Research Computing Service [Grant DOI: 10.14469/hpc/2232] and the Thomas Young Centre under Grant No. TYC-101.

## DATA AVAILABILITY

The data that support the findings of this article are not publicly available. The data are available from the authors upon reasonable request.

- 
- [1] I. Kirillov, I. Danilov, S. Sidorenkov, Y. Strebkov, R. Mattas, Y. Gohar, T. Hua, and D. Smith, Liquid lithium self-cooled breeding blanket design for iter, *Fusion Eng. Des.* **39–40**, 669 (1998).
  - [2] S. Konishi, M. Enoeda, M. Nakamichi, T. Hoshino, A. Ying, S. Sharafat, and S. Smolentsev, Functional materials for breeding blankets—status and developments, *Nucl. Fusion* **57**, 092014 (2017).
  - [3] S. Malang and R. Mattas, Comparison of lithium and the eutectic lead-lithium alloy, two candidate liquid metal breeder materials for self-cooled blankets, *Fusion Eng. Des.* **27**, 399 (1995).
  - [4] C. L. Guillaume, E. Gregoryanz, O. Degtyareva, M. I. McMahon, M. Hanfland, S. Evans, M. Guthrie, S. V. Sinogeikin, and H.-K. Mao, Cold melting and solid structures of dense lithium, *Nat. Phys.* **7**, 211 (2011).
  - [5] I. Tamblyn, J.-Y. Raty, and S. A. Bonev, Tetrahedral clustering in molten lithium under pressure, *Phys. Rev. Lett.* **101**, 075703 (2008).
  - [6] M. Hanfland, K. Syassen, N. E. Christensen, and D. L. Novikov, New high-pressure phases of lithium, *Nature (London)* **408**, 174 (2000).
  - [7] G. J. Ackland, M. Dunuwille, M. Martinez-Canales, I. Loa, R. Zhang, S. Sinogeikin, W. Cai, and S. Deemyad, Quantum and isotope effects in lithium metal, *Science* **356**, 1254 (2017).
  - [8] M. Hutcheon and R. Needs, Structural and vibrational properties of lithium under ambient conditions within density functional theory, *Phys. Rev. B* **99**, 014111 (2019).
  - [9] S. S. Behara, J. Thomas, and A. Van der Ven, Fundamental thermodynamic, kinetic, and mechanical properties of lithium and its alloys, *Chem. Mater.* **36**, 7370 (2024).
  - [10] A. Nichol and G. J. Ackland, Property trends in simple metals: An empirical potential approach, *Phys. Rev. B* **93**, 184101 (2016).
  - [11] W. S. Ko and J. B. Jeon, Interatomic potential that describes martensitic phase transformations in pure lithium, *Comput. Mater. Sci.* **129**, 202 (2017).

- [12] Z. Qin, R. Wang, S. Li, T. Wen, B. Yin, and Z. Wu, MEAM interatomic potential for thermodynamic and mechanical properties of lithium allotropes, *Comput. Mater. Sci.* **214**, 111706 (2022).
- [13] M. K. Phuthi, A. M. Yao, S. Batzner, A. Musaelian, B. Kozinsky, E. D. Cubuk, and V. Viswanathan, Accurate surface and finite-temperature bulk properties of lithium metal at large scales using machine learning interaction potentials, *ACS Omega* **9**, 10904 (2024).
- [14] Y. Zuo, C. Chen, X. Li, Z. Deng, Y. Chen, J. Behler, G. Csányi, A. V. Shapeev, A. P. Thompson, M. A. Wood, and S. P. Ong, Performance and cost assessment of machine learning interatomic potentials, *J. Phys. Chem. A* **124**, 731 (2020).
- [15] X. Wang, Z. Wang, P. Gao, C. Zhang, J. Lv, H. Wang, H. Liu, Y. Wang, and Y. Ma, Data-driven prediction of complex crystal structures of dense lithium, *Nat. Commun.* **14**, 2924 (2023).
- [16] D. K. Belashchenko and O. I. Ostrovskii, Application of the embedded atom model to liquid metals: Liquid lithium, *High Temp.* **47**, 211 (2009).
- [17] Z. Cui, F. Gao, Z. Cui, and J. Qu, Developing a second nearest-neighbor modified embedded atom method interatomic potential for lithium, *Modell. Simul. Mater. Sci. Eng.* **20**, 015014 (2012).
- [18] A. S. Al-Awad, L. Batet, and L. Sedano, Parametrization of embedded-atom method potential for liquid lithium and lead-lithium eutectic alloy, *J. Nucl. Mater.* **587**, 154735 (2023).
- [19] N. Artrith, A. Urban, and G. Ceder, Efficient and accurate machine-learning interpolation of atomic energies in compositions with many species, *Phys. Rev. B* **96**, 014112 (2017).
- [20] A. P. Bartók, M. C. Payne, R. Kondor, and G. Csányi, Gaussian approximation potentials: The accuracy of quantum mechanics, without the electrons, *Phys. Rev. Lett.* **104**, 136403 (2010).
- [21] J. Behler and M. Parrinello, Generalized neural-network representation of high-dimensional potential-energy surfaces, *Phys. Rev. Lett.* **98**, 146401 (2007).
- [22] A. Thompson, L. Swiler, C. Trott, S. Foiles, and G. Tucker, Spectral neighbor analysis method for automated generation of quantum-accurate interatomic potentials, *J. Comput. Phys.* **285**, 316 (2015).
- [23] Z. Li, J. R. Kermode, and A. De Vita, Molecular dynamics with on-the-fly machine learning of quantum-mechanical forces, *Phys. Rev. Lett.* **114**, 096405 (2015).
- [24] F. C. Mocanu, K. Konstantinou, T. H. Lee, N. Bernstein, V. L. Deringer, G. Csányi, and S. R. Elliott, Modeling the phase-change memory material,  $\text{Ge}_2\text{Sb}_2\text{Te}_5$ , with a machine-learned interatomic potential, *J. Phys. Chem. B* **122**, 8998 (2018).
- [25] M. Rupp, A. Tkatchenko, K.-R. Müller, and O. A. von Lilienfeld, Fast and accurate modeling of molecular atomization energies with machine learning, *Phys. Rev. Lett.* **108**, 058301 (2012).
- [26] S. Manzhos and T. Carrington, Jr., A random-sampling high dimensional model representation neural network for building potential energy surfaces, *J. Chem. Phys.* **125**, 084109 (2006).
- [27] A. V. Shapeev, Moment tensor potentials: A class of systematically improvable interatomic potentials, *Multiscale Model. Simul.* **14**, 1153 (2016).
- [28] A. Takahashi, A. Seko, and I. Tanaka, Conceptual and practical bases for the high accuracy of machine learning interatomic potentials: Application to elemental titanium, *Phys. Rev. Mater.* **1**, 063801 (2017).
- [29] M. A. Wood and A. P. Thompson, Extending the accuracy of the SNAP interatomic potential form, *J. Chem. Phys.* **148**, 241721 (2018).
- [30] R. Drautz, Atomic cluster expansion for accurate and transferable interatomic potentials, *Phys. Rev. B* **99**, 014104 (2019).
- [31] See Supplemental Material at <http://link.aps.org/supplemental/10.1103/q4nm-qyk4> for additional information including an introduction to ACE and other calculations, which also includes Refs. [78–81].
- [32] J. Nigam, S. N. Pozdnyakov, K. K. Huguenin-Dumittan, and M. Ceriotti, Completeness of atomic structure representations, *APL Mach. Learn.* **2**, 016110 (2024).
- [33] G. Dussan, M. Bachmayr, G. Csányi, R. Drautz, S. Etter, C. van der Oord, and C. Ortner, Atomic cluster expansion: Completeness, efficiency and stability, *J. Comput. Phys.* **454**, 110946 (2022).
- [34] Y. Lysogorskiy, C. v. d. Oord, A. Bochkarev, S. Menon, M. Rinaldi, T. Hammerschmidt, M. Mrovec, A. Thompson, G. Csányi, C. Ortner *et al.*, Performant implementation of the atomic cluster expansion (pace) and application to copper and silicon, *npj Comput. Mater.* **7**, 97 (2021).
- [35] G. Kresse and J. Hafner, *Ab initio* molecular-dynamics simulation of the liquid-metal–amorphous-semiconductor transition in germanium, *Phys. Rev. B* **49**, 14251 (1994).
- [36] P. E. Blöchl, Projector augmented-wave method, *Phys. Rev. B* **50**, 17953 (1994).
- [37] G. Kresse and J. Furthmüller, Efficient iterative schemes for *ab initio* total-energy calculations using a plane-wave basis set, *Phys. Rev. B* **54**, 11169 (1996).
- [38] J. P. Perdew, K. Burke, and M. Ernzerhof, Generalized gradient approximation made simple, *Phys. Rev. Lett.* **77**, 3865 (1996).
- [39] D. M. Ceperley and B. J. Alder, Ground state of the electron gas by a stochastic method, *Phys. Rev. Lett.* **45**, 566 (1980).
- [40] M. Methfessel and A. T. Paxton, High-precision sampling for Brillouin-zone integration in metals, *Phys. Rev. B* **40**, 3616 (1989).
- [41] M. Finnis and J. Sinclair, A simple empirical n-body potential for transition metals, *Philos. Mag. A* **50**, 45 (1984).
- [42] A. Bochkarev, Y. Lysogorskiy, S. Menon, M. Qamar, M. Mrovec, and R. Drautz, Efficient parametrization of the atomic cluster expansion, *Phys. Rev. Mater.* **6**, 013804 (2022).
- [43] Y. Lysogorskiy, A. Bochkarev, M. Mrovec, and R. Drautz, Active learning strategies for atomic cluster expansion models, *Phys. Rev. Mater.* **7**, 043801 (2023).
- [44] S. J. Plimpton, Fast parallel algorithms for short-range molecular dynamics, *J. Comput. Phys.* **117**, 1 (1995).
- [45] W. Swope, H. Anderson, P. Berens, and K. Wilson, A computer simulation method for the calculation of equilibrium constants for the formation of physical clusters of molecules: Application to small water clusters, *J. Chem. Phys.* **76**, 637 (1982).
- [46] S. Nose, A unified formulation of the constant temperature molecular-dynamics methods, *J. Chem. Phys.* **81**, 511 (1984).
- [47] M. Parrinello and A. Rahman, Polymorphic transitions in single crystals: A new molecular dynamics method, *J. Appl. Phys.* **52**, 7182 (1981).
- [48] A. Stukowski, Visualization and analysis of atomistic simulation data with OVITO—the open visualization tool, *Model. Simul. Mater. Sci. Eng.* **18**, 015012 (2010).

- [49] F. Mouhat and F. X. Coudert, Necessary and sufficient elastic stability conditions in various crystal systems, *Phys. Rev. B* **90**, 224104 (2014).
- [50] P. Jerabek, A. Burrows, and P. Schwerdtfeger, Solving a problem with a single parameter: A smooth bcc to fcc phase transition for metallic lithium, *Chem. Commun.* **58**, 13369 (2022).
- [51] F. Faglioni, B. V. Merinov, and W. A. I. Goddard, Room-temperature lithium phases from density functional theory, *J. Phys. Chem. C* **120**, 27104 (2016).
- [52] M. Hanfland, I. Loa, K. Syassen, U. Schwarz, and K. Takemura, Equation of state of lithium to 21 GPa, *Solid State Commun.* **112**, 123 (1999).
- [53] M. de Jong, W. Chen, H. Geerlings, M. Asta, and K. A. Persson, A database to enable discovery and design of piezoelectric materials, *Sci. Data* **2**, 150053 (2004).
- [54] H. Smith, R. Berliner, and J. Jorgensen, Martensitic transformation from bcc to 9R and FCC in metallic lithium, *Phys. B: Condens. Matter* **156–157**, 53 (1989).
- [55] L.-F. Zhu, P. Srinivasan, Y. Gong, T. Hickel, B. Grabowski, F. Körmann, and J. Neugebauer, Melting properties of the refractory metals V and W and the binary VW alloy fully from first principles, *Phys. Rev. B* **109**, 094110 (2024).
- [56] M. M. Beg and M. Nielsen, Temperature dependence of lattice dynamics of lithium 7, *Phys. Rev. B* **14**, 4266 (1976).
- [57] E. A. Owen and G. I. Williams, X-ray measurements on lithium at low temperatures, *Proc. Phys. Soc. Sec. A* **67**, 895 (1954).
- [58] H. C. Nash and C. S. Smith, Single-crystal elastic constants of lithium, *J. Phys. Chem. Solids* **9**, 113 (1959).
- [59] J. Trivisonno and C. S. Smith, Elastic constants of lithium-magnesium alloys, *Acta Metall.* **9**, 1064 (1961).
- [60] T. Slotwinski and J. Trivisonno, Temperature dependence of the elastic constants of single crystal lithium, *J. Phys. Chem. Solids* **30**, 1276 (1969).
- [61] D. M. Eike, J. F. Brennecke, and E. J. Maginn, Toward a robust and general molecular simulation method for computing solid-liquid coexistence, *J. Chem. Phys.* **122**, 014115 (2005).
- [62] A. Lazicki, Y. Fei, and R. J. Hemley, High-pressure differential thermal analysis measurements of the melting curve of lithium, *Solid State Commun.* **150**, 625 (2010).
- [63] P. S. Salmon, I. Petri, P. H. de Jong, P. Verkerk, H. E. Fischer, and W. S. Howells, Structure of liquid lithium, *J. Phys.: Condens. Matter* **16**, 195 (2004).
- [64] Y. Ito, K. Minami, and A. Nagashima, Viscosity of liquid lithium by an oscillating-cup viscometer in the temperature range 464–923 K, *Int. J. Thermophys.* **10**, 173 (1989).
- [65] R. K. Williams, G. L. Coleman, and D. W. Yarbrough, An evaluation of some thermodynamic and transport properties of solid and liquid lithium over the temperature range 200 to 1700 K, Tech. Rep. Oak Ridge National Lab, TN (USA) 1988, <https://www.osti.gov/biblio/5313590>.
- [66] R. W. Ohse, *Handbook of Thermodynamic and Transport Properties of Alkali Metals* (Blackwell Scientific Publications, 1991).
- [67] J. S. Murday and R. M. Cotts, Self-diffusion coefficient of liquid lithium, *J. Chem. Phys.* **48**, 4938 (1968).
- [68] P. I. Bystrov, D. N. Kagan, G. A. Krechetova, and E. E. Shpilrain, *Liquid-Metal Coolants for Heat Pipes and Power Plants* (Hemisphere Publishing, New York, 1990).
- [69] A. Y. Liu, A. A. Quong, J. K. Freericks, E. J. Nicol, and E. C. Jones, Structural phase stability and electron-phonon coupling in lithium, *Phys. Rev. B* **59**, 4028 (1999).
- [70] O. Blaschko, V. Dmitriev, G. Krexner, and P. Tolédano, Theory of the martensitic phase transformations in lithium and sodium, *Phys. Rev. B* **59**, 9095 (1999).
- [71] M. Krystian and W. Pichl, *In situ* optical microscopy of the martensitic phase transformation of lithium, *Phys. Rev. B* **62**, 13956 (2000).
- [72] M. Prem, M. Krystian, W. Pichl, G. Krexner, and S. Klotz, Neutron scattering investigation of pressure-induced phase transitions in Li and Ba, *J. Phys.: Condens. Matter* **17**, S3165 (2005).
- [73] M. Islam, J. Lore, S. Smolentsev, and C. Kessel, Divertor geometry modeling with the SOLPS-ITER code for reactor concepts with liquid metal divertors, *Nucl. Mater. Energy* **33**, 101292 (2022).
- [74] B. Deng, P. Zhong, K. Jun, J. Riebesell, K. Han, C. Bartel, and G. Ceder, CHGNet as a pretrained universal neural network potential for charge-informed atomistic modelling, *Nat. Mach. Intell.* **5**, 1031 (2023).
- [75] A. Bochkarev, Y. Lysogorskiy, and R. Drautz, Graph atomic cluster expansion for semilocal interactions beyond equivariant message passing, *Phys. Rev. X* **14**, 021036 (2024).
- [76] I. Batatia, S. Batzner, D. P. Kovács, A. Musaelian, G. N. C. Simm, R. Drautz, C. Ortner, B. Kozinsky, and G. Csányi, The design space of E(3)-equivariant atom-centered interatomic potentials, *arXiv:2205.06643*.
- [77] M. Neumann, J. Gin, B. Rhodes, S. Bennett, Z. Li, H. Choubisa, A. Hussey, and J. Godwin, Orb: A fast, scalable neural network potential, *arXiv:2410.22570*.
- [78] W. A. Harrison, Multi-ion interactions and structures in simple metals, *Phys. Rev. B* **7**, 2408 (1973).
- [79] F. H. Stillinger and T. A. Weber, Computer simulation of local order in condensed phases of silicon, *Phys. Rev. B* **31**, 5262 (1985).
- [80] M. Mendelev, M. Kramer, C. A. Becker, and M. Asta, Analysis of semi-empirical interatomic potentials appropriate for simulation of crystalline and liquid Al and Cu, *Philos. Mag.* **88**, 1723 (2008).
- [81] S. A. Etesami and E. Asadi, Molecular dynamics for near melting temperatures simulations of metals using modified embedded-atom method, *J. Phys. Chem. Solids* **112**, 61 (2018).